







# Dynamics of Descending Knots in a Solar Prominence and Their Possible Contributions to the Heating of the Local Corona

Yi Bi<sup>1,2,3</sup> , Bo Yang<sup>1,3</sup> , Ting Li<sup>2,4</sup> , Yan Dong<sup>1,3</sup>, and Kaifan Ji<sup>1,3</sup> 

<sup>1</sup> Yunnan Observatories, Chinese Academy of Sciences, 396 Yangfangwang, Guandu District, Kunming 650216, People's Republic of China; [biyi@ynao.ac.cn](mailto:biyi@ynao.ac.cn)

<sup>2</sup> Key Laboratory of Solar Activity, National Astronomical Observatories of Chinese Academy of Science, Beijing 100012, People's Republic of China

<sup>3</sup> Center for Astronomical Mega-Science, Chinese Academy of Sciences, 20A Datun Road, Chaoyang District, Beijing 100012, People's Republic of China

<sup>4</sup> School of Astronomy and Space Science, University of Chinese Academy of Sciences, Beijing 100049, People's Republic of China

Received 2019 December 4; revised 2020 February 11; accepted 2020 February 20; published 2020 March 13

## Abstract

The knots in solar prominences are often observed to fall with nearly constant velocity, but the associated physical mechanism is currently not well understood. In this Letter, we present a prominence observed by the New Vacuum Solar Telescope in  $H_{\alpha}$  wavelength. Knots that rose within the prominence appear to have been preferentially located at higher altitude, whereas those that fell were found throughout the entire prominence structure. The descending speed of the knots near the solar surface was higher than that far away from the solar surface. We noted that the knots near the solar surface may run along a set of coronal loops observed from the Atmospheric Imaging Assembly. Elsewhere, the majority of knots are interpreted to have descended across more horizontal magnetic fields with a nearly constant speed. This lack of acceleration indicates that the liberated gravitational potential energy may not manifest as an increase in kinetic energy. Assuming instead that the descending knots were capable of exciting Alfvén waves that could then dissipate within the local corona, the gravitational potential energy of the knots may have been converted into thermal energy. Assuming a perfectly elastic system, we therefore estimate that the gravitational energy loss rate of these observed knots amounts to  $\approx 1/2000$  of that required to heat the entire quiet Sun, increasing to  $1/320$  when considering possibly further downward motions of the knots having disappeared in the  $H_{\alpha}$  observations. This result suggests such a mechanism may contribute to the heating of the corona local to these prominences.

*Unified Astronomy Thesaurus concepts:* [The Sun \(1693\)](#); [Solar prominences \(1519\)](#); [Solar chromosphere \(1479\)](#); [Solar coronal heating \(1989\)](#); [Solar corona \(1483\)](#); [Solar filaments \(1495\)](#); [Solar magnetic fields \(1503\)](#); [Solar physics \(1476\)](#)

*Supporting material:* animation

## 1. Introduction

Solar prominences are the plasma structures with high density and low temperature in the tenuous and hot corona (Labrosse et al. 2010; Mackay et al. 2010). The so-called hedgerow-type prominence is the quiescent prominence that consists of long and tall blade-like palisades (Engvold 2015). Observations have shown that the plasma within such prominences typically exhibits both vertical and horizontal flows of the order of tens of  $\text{km s}^{-1}$  (Engvold 1976; Chae 2010; Liu et al. 2012). Similar to the bidirectional pattern of flows found in a filament (Zirker et al. 1998), persistent horizontal flows that may reach long distances can be detected in hedgerow prominences (Chae et al. 2008). However, of particular interest are the thin, downward-directed mass flows with velocities much less than freefall speeds. The observational study by Liu et al. (2012) led the authors to suggest that the entire mass of a prominence could be swapped out on the order of a day by these vertical flows. The mechanism responsible for then replenishing the drained prominence material has been suggested to be some form of coincident condensation process (e.g., Antiochos et al. 1999; Keppens et al. 2015; Xia & Keppens 2016) or a consequence of the draining material interacting with the transition region via the Rayleigh–Taylor instability (RTI; see, e.g., Keppens et al. 2015; Kaneko & Yokoyama 2018). The RTI has also previously been invoked to explain the thin rising plumes that are typically coincident with the aforementioned falling structures (e.g., Hillier et al. 2012), not to be confused with the large *voids* that have been observed

to grow beneath prominences and are believed to be associated with flux emergence (e.g., Berger et al. 2010).

The horizontal flows seen in the prominence are often interpreted as observational evidence that the plasma is supported by the sagging of initially horizontal magnetic field lines (Chae et al. 2008; Shen et al. 2015). As such, it remains an open question as to how the knots observed to fall may do so through a medium permeated by horizontal magnetic fields. Low et al. (2012) suggested that a downward resistive flow across the supporting horizontal field is a result of developing of a mass sheet singularity under the falling knots, while Chae (2010) proposed instead that magnetic reconnection takes place around the descending knots. However, Haerendel & Berger (2011) suggested that the horizontal orientation of the external field is rather unfavorable for magnetic reconnection with the knots. Assuming that the plasma packet constituting the knots has a very high value of beta, the author suggested that the knots will behave like a diamagnetic body, which deforms the ambient field as it slips through it. The downward acceleration is then counterbalanced by a friction force due to dissipation of Alfvén waves along the horizontal magnetic field, and then the downward motions keep almost a constant speed.

If the falling knots travel with constant downward speed along more vertical magnetic fields, a hydrostatic pressure gradient could provide an upward force that may balance the force of gravity acting on the falling knots. Modeling the evolution of a density enhancement in a stratified atmosphere with uniform magnetic field, Mackay & Galsgaard (2001) found that this

pressure gradient can build up under the density enhancement, causing it to fall through the stratified atmosphere with speeds much less than the freefall speed. Similarly, Oliver et al. (2014) investigated the dynamical evolution of a fully ionized plasma blob in an isothermal, vertically stratified corona. The authors found that the presence of a heavy condensation gave rise to the formation of a large pressure gradient that opposed gravity, and eventually this pressure gradient became so large that the blob acceleration vanished. In the model proposed by Low et al. (2012), the liberated energy is converted to dissipative energy that fuels the radiative loss of the prominence plasma. By contrast, Haerendel & Berger (2011) suggested that the Alfvén waves excited by the falling knots carry away the liberated energy.

Coronal heating is a topic dedicated to explaining how the corona may be heated up to a temperature of millions of degrees, far above that of the photosphere. Alfvén-wave turbulence is a promising candidate to transport magneto-convective energy upward along the Sun’s magnetic field lines into the corona. McIntosh et al. (2011) detected Alfvénic waves in type II spicules, which could be energetic enough to heat the quiet corona. Samanta et al. (2019) showed the evidence that these spicules may originate from the solar surface. However, some further investigations showed that the wave energy communicated by spicules was in actual fact far less than that required to heat the corona of the quiet Sun (Thurgood et al. 2014; Weberg et al. 2018). As another candidate for heating the corona, the nanoflare proposal suggested by Parker (1988) involved the slow braiding of coronal field lines and the impulsive release of stored energy. Using high-resolution coronal imager instrument on board a rocket, Cirtain et al. (2013) suggested the magnetic braids in a coronal active region that are reconnecting, relaxing, and dissipating sufficient energy to heat the corona. However, the braiding and relaxation are not immediately obvious as noted by Zirker & Engvold (2017). The magnetic reconnection associated with the newly emergence flux may also contribute to heat the quiet Sun (Close et al. 2005; Zhang et al. 2015).

In this study, we have investigated the vertical motion of  $H_\alpha$  knots within a solar prominence observed using the New Vacuum Solar Telescope (NVST; Liu & Beckers 2001; Liu et al. 2014). We have identified the rising and descending knots in the presented prominence, before estimating the velocity and acceleration of the knots on the plane of sky. This allows us to investigate the spatial distribution of temporal kinetics of the knots. Furthermore, we have roughly estimated the loss rate of the gravitational potential from the descending knots and compared it with heating power requirement for the corona in the quiet Sun.

## 2. Observation and Data Analysis

### 2.1. Overview of the Observation

NVST is a ground-based multichannel high-resolution imaging system, including  $H_\alpha$ ,  $G$ -band, TiO-band, and Ca II 8542 Å wavelengths. The studied prominence, located on the west limb of the Sun, was observed by NVST from 02:20 to 07:10 UT on 2017 January 7. During this period, NVST provided the  $H_\alpha$  linecore image with a prefilter width of 0.25 Å. These images have a temporal cadence of 11 s, a spatial sampling of  $0''.16$ , and a field of view (FOV) of  $153'' \times 153''$ . A high-resolution NVST image is normally reconstructed from at

least 100 short-exposure images. After reconstruction (Xiang et al. 2016), the actual resolution of an image of the chromosphere ( $H_\alpha$ , 6563 Å) is better than  $0''.3$ . With such a spatial resolution, NVST can resolve many fundamental structures in the photosphere and chromosphere within a  $3'$  FOV (Xu et al. 2014).

The observed prominence in an  $H_\alpha$  image has a length of  $\sim 80$  Mm and an upper extent of  $\sim 80$  Mm. Figure 1(a) presents an  $H_\alpha$  image that is aligned to the full-disk GONG  $H_\alpha$  image, which has a spatial sampling of  $1''.0$ .

The Atmospheric Imaging Assembly (AIA; Lemen et al. 2012) on board the *Solar Dynamic Observatory* (SDO; Pesnell et al. 2012) provides full-disk images of the corona with a spatial sampling of  $0''.6$ . Comparing the  $H_\alpha$  image with AIA/304 Å image (Figure 1(c)), we can see that the prominence observed in  $H_\alpha$  is the northern part of a larger prominence in the 304 Å image.

As shown in the bottom panels of Figure 1, the images were rotated to ensure that the photospheric limb is horizontal. The AIA 211 Å image (Figure 1(f)) that is taken at the same time with the NVST  $H_\alpha$  image (Figure 1(g)) shows that a set of coronal loops appears under the prominence on the limb. Taken at an earlier time, the 211 Å image presents that the coronal arcades (denoted by the arrow in Figure 1(e)) seem to be located around one endpoint of the prominence (Figure 1(e)). Based on a high-accuracy solar image registration procedure (Feng et al. 2012; Yang et al. 2014), all of the NVST images are aligned to the same FOV as indicated by Figure 1(g). This will allow us to study the motions of the structures detected in the NVST images.

### 2.2. The Technique of Optical Flow

Time sequences of high-cadence images enable the identification and study of the dynamics features across the image plane. The optical flow, referring to the proper motion of a feature across the image plane, may be used to determine the velocity field from two images. The technique of local correlation tracking (LCT; November & Simon 1988) and the differential affine velocity estimator (DAVE; Schuck 2006) are two kinds of optical flow techniques that have been widely used in the solar research.

Thirion (1988) presented a model to perform image-to-image matching by determining the optical flow between two images. The author illustrated the concept of this model by an analogy with Maxwell’s demons, as such this algorithm is usually named as nonrigid Demon algorithm. Liu et al. (2018) have examined the performance of three different methods (Demon, DAVE, and LCT) using a photosphere and chromosphere image provided by NVST. After shifting the images 5.6 pixels in the  $x$  direction and 0.2 pixels in the  $y$  direction, they noted that the Demon found displacements that are closer to the *true* displacements and then they suggested that the Demon algorithm outperformed traditional LCT and DAVE methods in estimating the analog displacements both smaller and larger than 1 pixel.

Here, we used both the DAVE and Demon algorithms to obtain the optical flow between two NVST  $H_\alpha$  images. The earlier image is set as the reference image and the later image as the target image. As an example, Figure 2(a) shows a reference image and Figure 2(d) shows the difference image between the reference and target image. The DAVE and Demon velocity fields are indicated by arrows in Figures 2(b) and (c), respectively. To test the performance of each technique, we warped the reference image to

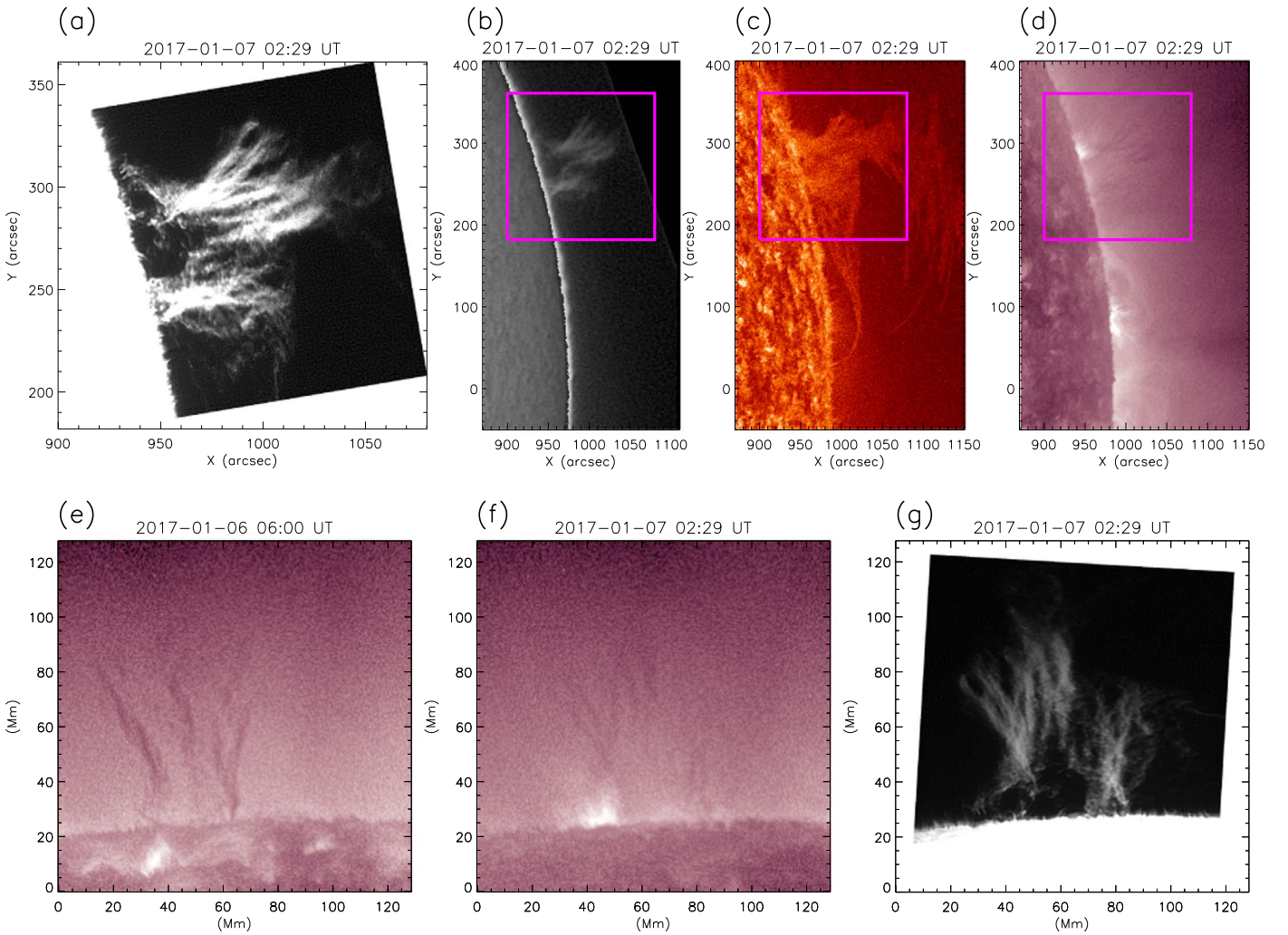


**Figure 1.** (a, g) NVST  $H_{\alpha}$  image. (b) GONG  $H_{\alpha}$  image. (c) AIA 304  $\text{\AA}$  image. (d–f) AIA 211  $\text{\AA}$  image. The pink boxes in the three top panels indicate the position and FOV of panel (a), which is the full view of the NVST. The images in the bottom panels (e–g) are rotated so that the photospheric limb is horizontal. Each AIA image was enhanced by using the Multiscale Gaussian Normalization technique (Morgan & Druckmüller 2014), which is very effective at revealing faint fine-scale details of the prominence studied here.

align with the target image based on the resulting optical flow. Ideally, the warped image would be identical to the target image. Figures 2(e) and (f) present the difference image between the target image and the warped image based on DAVE (Demon). Comparing the warping image based on DAVE, the Demon-based warping image has less difference from the target image. Based on these results, the Demon-based optical flow is chosen to study the velocity of the knots in the prominence. As shown in the A.1, the errors of the velocities measured by Demon is about  $2 \text{ km s}^{-1}$ .

### 2.3. Identifying and Tracking Knots

Different from the vertical thread in the prominence, the bright knots appear to be brighter and shorter in the vertical direction. Here, we used a morphological approach to identify the rising or descending knots in the prominence. First, since the bright knots are located on a nonuniform background, contrast of the  $H_{\alpha}$  image was enhanced using contrast-limited adaptive histogram equalization (CLAHE; Zuiderveld 1994). Figure 3(a) presents one of the enhanced  $H_{\alpha}$  images. A representative bright knot is denoted by the arrow in Figure 3(a). Second, to further enhance contrast of the bright knots on the images, we performed morphological top-

hat filtering on the enhanced  $H_{\alpha}$  image; the bright knots were then separated from the background (Figure 3(b)). Based on a threshold of intensity value on the top-hat transformed image, the bright knots can be identified, as the color (magenta and green) contours outline (Figure 3(b)). Third, to distinguish between the rising and falling blobs, and other uninteresting features, we selected the structures that have a vertical displacement larger than its initial vertical extent. As shown in Figure 3(b), the magenta contours denote the rising or descending bright knots that are selected, while the uninteresting features are colored green. Each point in Figure 3(c) denotes the location where each knot starts to be identified. The knots with rising and descending motions are colored red and blue, respectively. It is obvious from the distribution of points that the rising knots are often located in the higher altitude, while the descending motions are in the low altitude. In Figure 3(d), the identified knots are colored based on the vertical velocity estimated from Demon.

## 3. Results

Applying the algorithm outlined above to the  $H_{\alpha}$  images, we identified and tracked 6194 moving bright knots. The widths of the knots range from 1 to 3 Mm (Figure 4(a)). The heights of

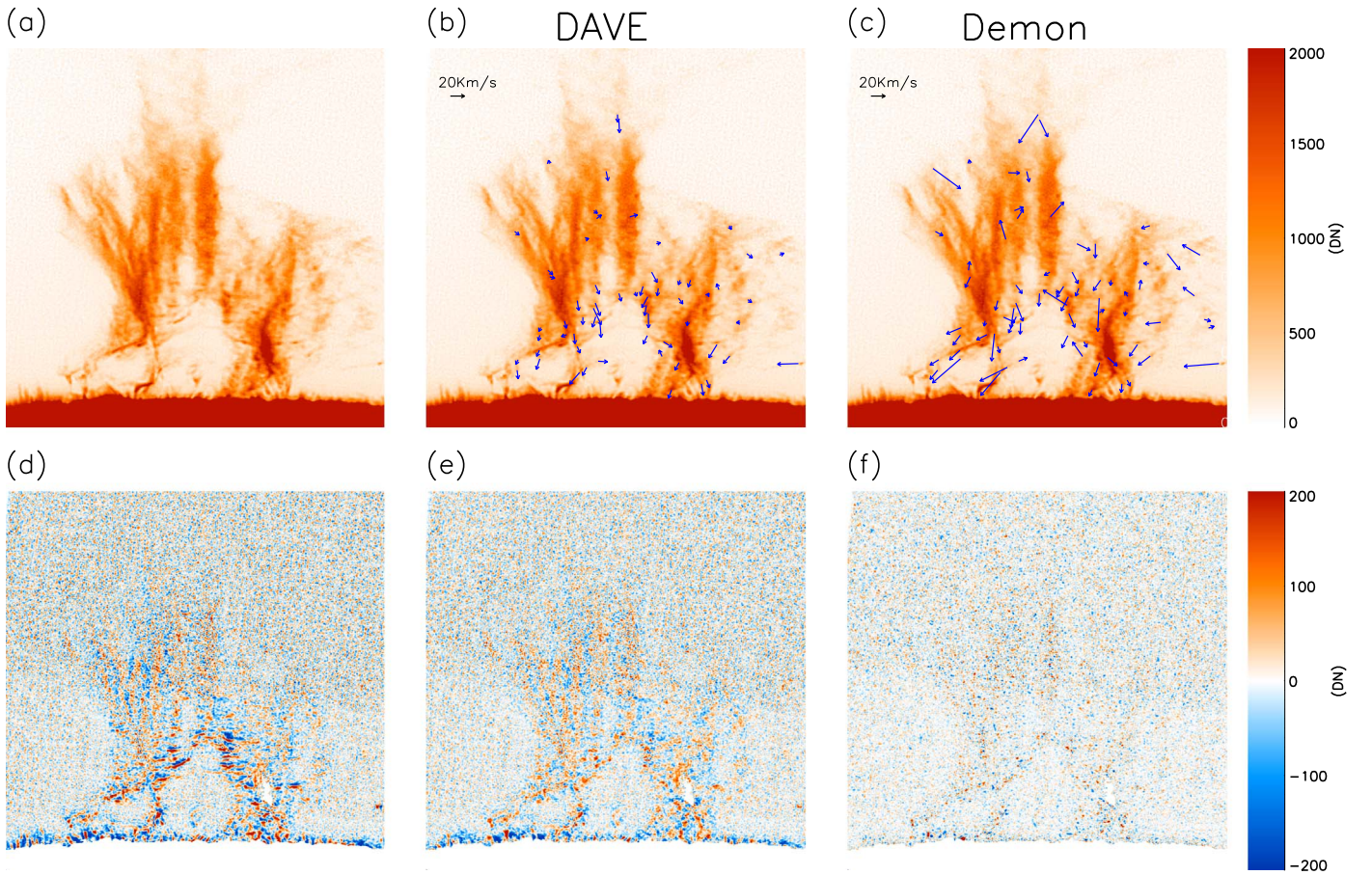


**Figure 2.** (a–c) NVST  $H_\alpha$  images taken at 02:22:29 UT. (d) The difference image between the reference and target image, which refers to the NVST  $H_\alpha$  images taken at 02:22:29 UT and 02:22:51 UT, respectively. In panels (b) and (c), the arrows indicate the optical flow based on techniques of DAVE and Demon, respectively. (e, f) The difference images between the reference and warping image. In panels (e) and (f), the warping image refers to the reference image that is warped to align with the target image based on the optical flows of DAVE and Demon, respectively.

the knots to solar surface range from 2 to 85 Mm (Figure 4(b)). Among these tracked knots, 4655 knots show downward motions, and the remaining 1539 knots show upward motions. The knots travel upward or downward with a vertical distance of several Mm (Figure 4(c)). Figure 4(c) shows the distribution of the vertical distances that the knots traveled. Here, positive and negative values mean that the knot has experienced a downward and upward motion, respectively. We found that the majority of knots disappeared from the  $H_\alpha$  image after rising or falling less than 4 Mm. These knots are visible in less than 10  $H_\alpha$  images and their lifetimes range from 1 to 2 minutes. However, 713 of the 4655 downward knots were detected to travel longer than 4 Mm in the vertical direction, among which 75 knots descend more than 10 Mm.

The velocity of a knot is estimated by averaging the Demon velocities of the knot detected at different times. The histogram in Figure 4(d) shows the vertical velocity distribution for the identified knots. Again, more knots are found to display downward velocity. The descending knots fall at the speed of about  $18 \text{ km s}^{-1}$ , while the other knots rise at the lower speed of  $10 \text{ km s}^{-1}$ .

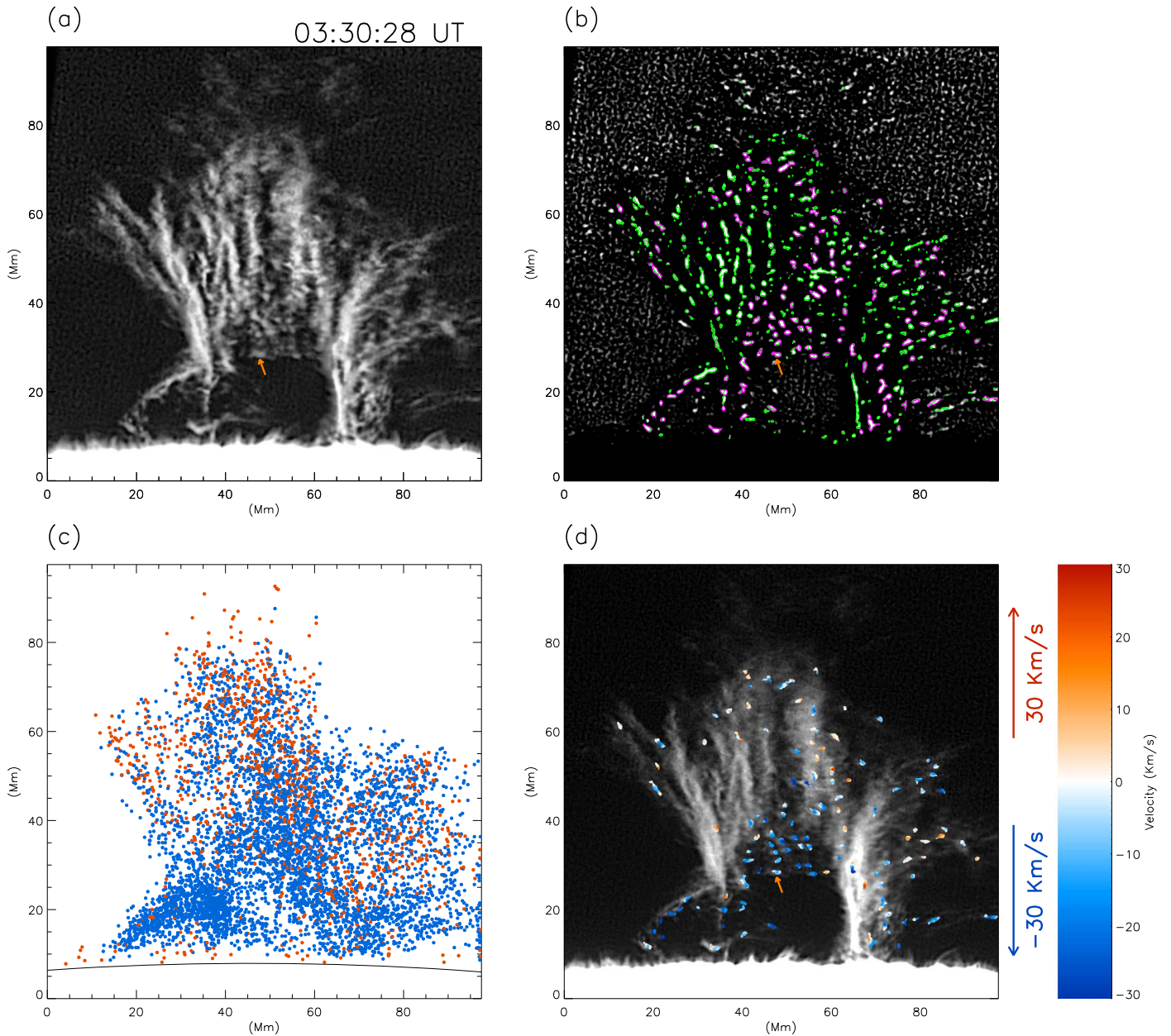
The acceleration  $a$  of a knot is obtained by a least-squares linear fit for the velocity, such as  $V_{\text{fit},i} = av_i + b$ , where  $v_i$  is the vertical velocity of a knot observed in the  $i$ th moment. The histogram of  $a$  (Figure 4(e)) shows that the distribution of knot acceleration peaks at a value of zero with an FWHM of only  $0.42g_{\text{Sun}}$ , where  $g_{\text{Sun}} = 0.272 \text{ km s}^{-2}$  near the solar surface.

Figure 4(g) presents the histogram of the brightness of knots. Again, the brightness of a knot is defined as the average of that of the knot detected at different moments. We defined the change rate of the brightness of an identified knot as  $\Delta B = (B_{\text{fit},N} - B_{\text{fit},1})/\bar{B}_{\text{fit}}$ , where  $B_{\text{fit},i} = ab_i + b$  is a linear fit to the brightness  $b_i$  of a knot detected at the  $i$ th image,  $i = 1, 2, \dots, N$ , and a knot is identified in  $N$  images. The  $\Delta B$  greater than zero means that the total brightness increases when a knot rises or descends, while  $\Delta B$  lower than zero indicates the brightness decreases. The histogram in Figure 4(h) shows that the distribution of  $\Delta B$  is close to a Gaussian profile with a peak at  $-0.10$ , indicating that the number of knots whose brightness decreases over time is slightly bigger.

It is worth noting that, however, the knots disappeared in the  $H_\alpha$  image after the knots were traced in several or more images. In order to isolate the final velocity and the brightness of the knots that were recognized in the  $H_\alpha$  images, we defined

$$\Delta v_{\text{end}} = \frac{v_{\text{end}} - V_{\text{fit, end}}}{V_{\text{fit, end}}}, \quad \Delta b_{\text{end}} = \frac{b_{\text{end}} - B_{\text{fit, end}}}{B_{\text{fit, end}}}, \quad (1)$$

where the term “end” denotes the image in which a knot was recognized at the last time. The larger value of  $\Delta v_{\text{end}}$  ( $\Delta b_{\text{end}}$ ) indicates a larger change in the vertical velocity (total brightness) of a knot before it disappears. The histogram of  $\Delta v_{\text{end}}$  (Figure 4(f)) shows a Gaussian profile with peak at  $-0.1$ , while the histogram of  $\Delta b_{\text{end}}$  (Figure 4(i)) fits a Gaussian distribution with the peak at



**Figure 3.** (a) NVST  $H_{\alpha}$  image that is CLAHE enhanced. (b) The identified bright knots are outlined with color contours. The megacontours refer to the knots that have a value of vertical displacement larger than the height of the knots themselves. The green contours denote the left knots. (c) Each point denotes the location where each knot starts to be identified. The red and blue points indicate the knots that show rising and descending motions, respectively. The dark line denotes the solar limb. (d) The identified knots are colored based on the value of vertical Demon velocity. In each panel, the orange arrow denotes a knot as an example. Slightly different from this figure, panel (c) in the animation displays the trajectories of the running knots, but in which the red and blue also denote the rising and descending motions, respectively. The animation begins at 02:22:51 UT and ends at 07:09:15 UT. The real-time duration of the video is 58 s.

(An animation of this figure is available.)

-0.39. Therefore, at a time when these knots were about to disappear on the  $H_{\alpha}$  image, the brightness of knots decreased impulsively, but their descending velocity did not change significantly. It implies that the knots may keep falling after they cannot be identified in the  $H_{\alpha}$  images.

Figure 5(a) shows an averaged  $H_{\alpha}$  image, in which each pixel is an average of the brightness of the knots that are detected at the same location at different times. Similarly, Figures 5(b) and (c) show the averaged Demon velocity distribution of the knots in the horizontal and vertical directions, respectively. Figure 5(b) shows that the horizontal velocity is close to  $30 \text{ km s}^{-1}$  on the

bottom of the prominence and is greater than  $5 \text{ km s}^{-1}$  in most areas at higher altitude. In Figure 5(c), the upward vertical velocity could be found predominantly in the upper portions of the prominence, whereas the downward velocity was present at seemingly all altitudes with the strongest signatures at the bottom of the prominence.

To detail the value of the speed of the falling knots, Figure 5(e) shows the distribution of the vertical velocity in the downward direction. In the area denoted by the box in Figure 5(e), the downward velocity of the knots is greater than  $25 \text{ km s}^{-1}$ . Comparing to the FOV of AIA 211 Å, the box

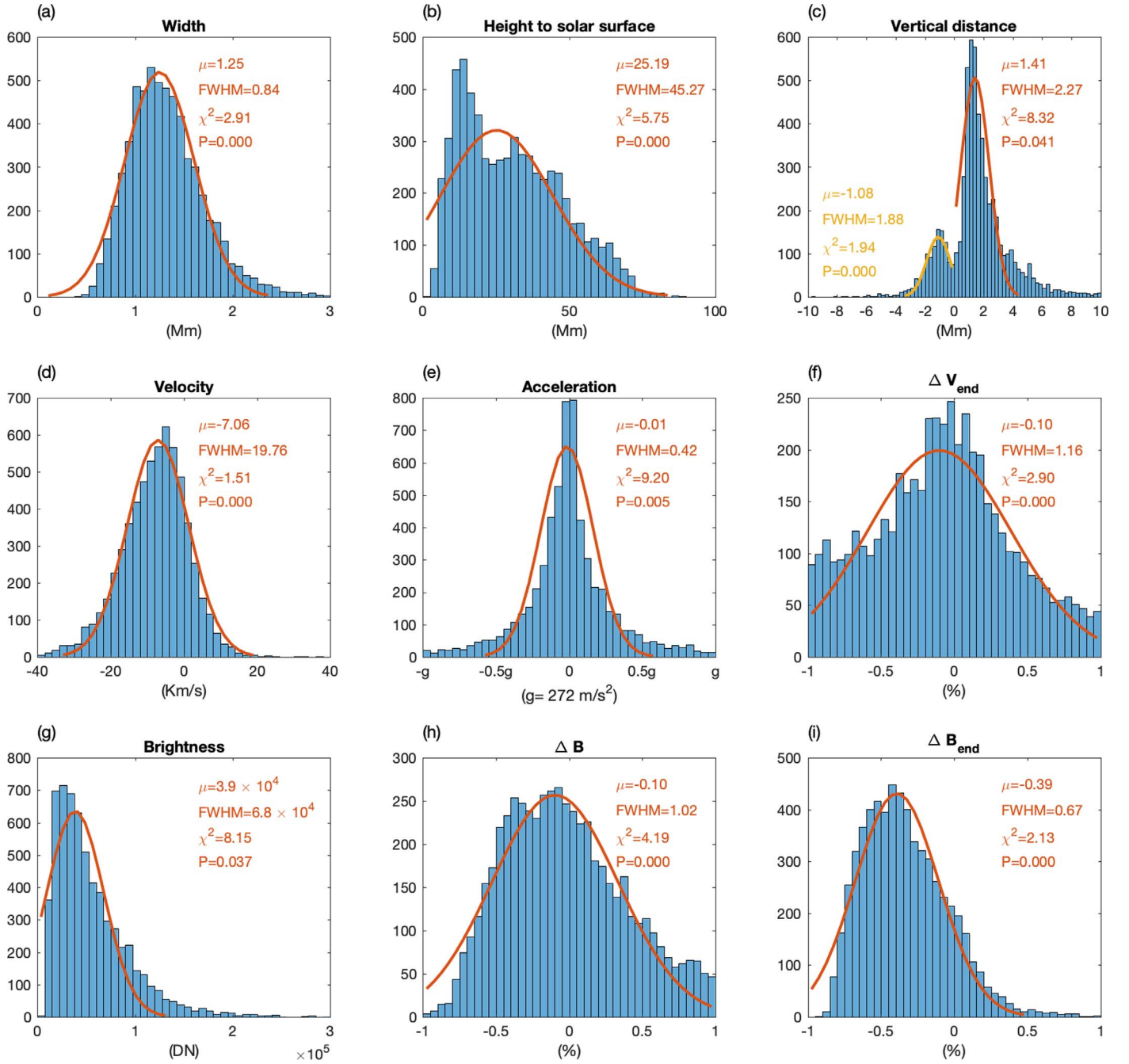


**Figure 4.** Histograms showing the distributions of width (a), the height to the solar surface (b), vertical distance of fall (c), vertical velocity (d), vertical acceleration (e),  $\Delta V_{\text{end}}$  (f), brightness (g),  $\Delta B$  (h), and  $\Delta B_{\text{end}}$  (i) of the identified knots, respectively. In each panel, the line represents the central part of a Gaussian function  $\mathcal{N}(\mu, \sigma^2)$  fitting the main part of binned data. The fitting parameters are shown in each panel, including the parameter  $\mu$ , FWHM of  $\sim 2.35\sigma$ , chi-square ( $\chi^2$ ), and  $P$ -value of each fitting. In general, we regard the Gaussian function as a suitable fit to the data if its  $P$ -value is smaller than 0.05. Accordingly, the Gaussian shape is a reasonable assumption for the main part of each distribution.

covers a set of coronal loops (Figure 5(d)). It is thus possible that the quickly falling knots may run along the magnetic field that is marked by the coronal loops. The majority of knots outside the box were found to descend with a velocity lower than  $25 \text{ km s}^{-1}$ . Overall, the largest downward velocities were located at the bottom of the prominence.

The acceleration of a knot was estimated from the result of linear fit to the vertical speed of an identified knot in three moments. The map in Figure 5(f) then presents averaged acceleration of the identified knots, in which the dashed line denotes the height of 7 Mm above the solar surface. The

majority of the knots at a height above 7 Mm appear to have had a downward acceleration much less than the gravitational acceleration experienced at the solar surface. However, within about 7 Mm above solar surface, the knots underwent a rapid deceleration, with the value of acceleration as high as  $-g_{\text{sun}}$ .

#### 4. Discussions

In this study, we have identified and tracked the knots within a solar prominence that was observed by the NVST. Although knots were observed to have propagated both upward and

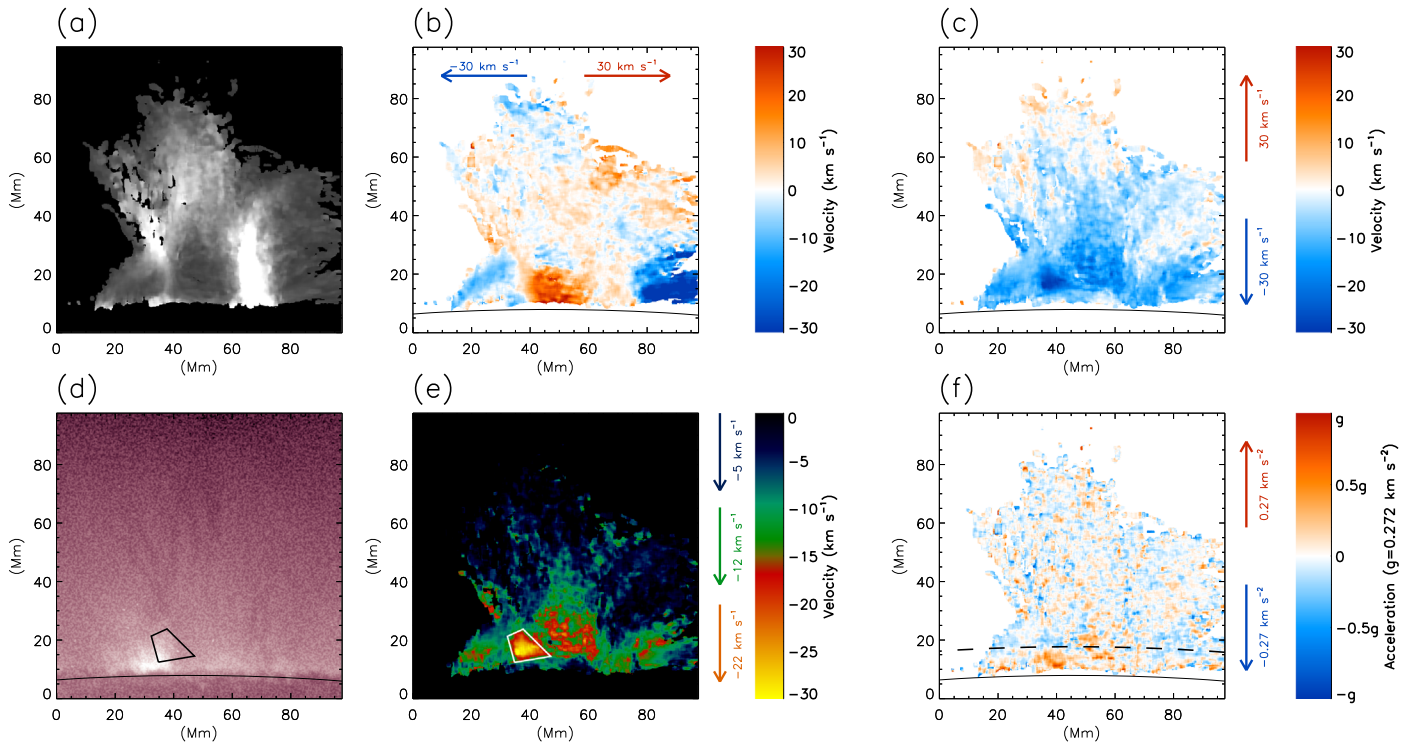


**Figure 5.** Maps of averaged brightness (a), vertical velocity (b), horizontal velocity (c), downward velocity (e), and vertical acceleration (f) of the identified knots. In these maps, the value in each pixel is an average of the values in each pixel at different times. (d) AIA/211 Å image. In panel (f), the dashed line indicates a line with height of 7 Mm above the solar surface.

downward (with respect to the solar surface), a larger percentage of the motions were recorded in the downward direction. These upward motions may be a consequence of the initially downward-directed motions (see the RTI as explored by, e.g., Keppens et al. 2015), and we may in turn speculate that this explains their prevalence at the upper levels within the prominence. However, in the absence of additional information we continue below with a focus on the more common downward motions.

By identifying and tracking the descending knots in the prominence, we found that the knots reached a higher speed in the low altitude. The knots that reached the maximum speed of  $30 \text{ km s}^{-1}$  were cospatial with a set of coronal loops observed in AIA 211 Å, thereby it is possible that the knots with high speed fell along the magnetic field lines denoted by the observed loops. If so, the gravity acted on the knots may be balanced by the pressure gradient when the knots descended along the magnetic field (Mackay & Galsgaard 2001). However, as discussed below, this picture may not sufficiently explain the motions of the knots such as those with a lower downward speed at higher altitudes.

Falling through the stratified atmosphere threaded with a vertical magnetic field, a knot is expected to achieve greater speed if its density is higher or it falls in a rarer environment (Oliver et al. 2014). Assume that each knot is optically thin in  $H_{\alpha}$ , the higher density of a knot in the same altitude would be brighter in  $H_{\alpha}$  images (Heinzl et al. 2015). However, no evidence showed that the knots having higher descending speed had higher density, because that the brightness of the knots did not have the correlation to the vertical velocity of the knots. On the other hand, a vertically stratified corona has the vertical scale height of about 120 Mm. It means that,

with the height of 80 Mm, the density of the corona in the high altitude is significant rarer than in the low altitude. Therefore, it is expected that the knots in the high altitude could reach a higher downward speed if all of the knots fall along the vertical magnetic field in the stratified corona, which is contradictory to the observation presented here. Instead, we are inclined to view that most of the knots fell across more horizontal fields as suggested in Mackay & Galsgaard (2001). This is particularly important for those knots that were not co-located with the loops viewed in AIA 211 Å.

The descending knots were measured to have fallen at speeds of approximately  $18 \text{ km s}^{-1}$ , which is consistent with previously established observational values of  $10\text{--}15 \text{ km s}^{-1}$  (Berger et al. 2008; Chae 2010; Li et al. 2018). Using a three-dimensional MHD simulation including optically thin radiative cooling and nonlinear anisotropic thermal conduction, Kaneko & Yokoyama (2018) found that the downward speed of the dense plasma is approximately  $12 \text{ km s}^{-1}$ . In the prominence studied here, a few knots fell at speed as high as about  $40 \text{ km s}^{-1}$ . Freed et al. (2016) reported on vertical plasma motions within prominences that reached magnitudes up to  $30 \text{ km s}^{-1}$ , although the authors also noted that the FLCT method systematically underestimates the true velocity. MHD modeling of prominence dynamics also indicated downward motions of dense plasma at up to  $60 \text{ km s}^{-1}$  prevailed instantaneously (Keppens et al. 2015).

Since the knots displayed an approximately constant downward motion, most of the liberated gravitational potential energy may not have manifested itself as an increase in kinetic energy. As suggested by Low et al. (2012), if the knots flow downward across the supporting magnetic field, the liberated gravitational potential energy could be conserved into dissipative energy that fuels the radiative loss of the prominence plasma. Based on the

model proposed by Haerendel & Berger (2011), the descending knots would excite the Alfvén wave propagating along the horizontal magnetic field. It means that the gravitational potential energy could be converted into the wave energy, which may contribute to the heating of the corona in the quiet Sun.

The loss of the gravitational potential energy is equal to  $Mg_{\text{Sun}}h$ , where  $g_{\text{Sun}}$  is the gravitational acceleration of  $0.272 \text{ km s}^{-2}$  near the solar surface. In the present study, we took  $h$  as the distance from which an identified knot had fallen. The mass of a cool prominence is roughly equal to  $M \approx 1.4N_{\text{H}}m_{\text{H}}V$  (Heinzel et al. 1996), where  $N_{\text{H}}$  and  $m_{\text{H}}$  are the mean neutral hydrogen number density and the mass of the hydrogen atom, respectively, and  $V$  is the volume occupied by the prominence plasma.

The literature values of the electron density within the prominence varied greatly and within a range of  $10^9$ – $10^{11} \text{ cm}^{-3}$  (Labrosse et al. 2010). Some of these variations were, undoubtedly, due to differences between the various techniques that are used, but there were likely to also be variations between parts of the same prominence. Unfortunately, few studies have focused specifically on the density of the knots observed within solar prominences. Assuming that the knots have a high-beta magnetic structure, Haerendel & Berger (2011) estimated that the peak density of the knots must be as high as  $3 \times 10^{12} \text{ cm}^{-3}$  with an average density of  $5 \times 10^{11} \text{ cm}^{-3}$ . Accordingly, we take the density of the knots as  $5 \times 10^{11} \text{ cm}^{-3}$ . To determine the volume of the knots, we assume that the length of the knots in the line of sight has the same scale with that in the plane of sky. Based on the above assumptions, the loss of gravity potential energy from the detected falling knots is about  $5.3 \times 10^{21} \text{ erg}$  during the period of  $\sim 5 \text{ hr}$ . This is equivalent to a potential energy loss rate of  $3 \times 10^{17} \text{ erg s}^{-1}$  for the falling knots in this prominence.

We assume that the majority of the knots were not falling through an additional prominence magnetic field, but instead across the horizontal field of the background corona. This implies that the converted gravitational energy is not contributing to the heating within the prominence itself. Under this assumption, it is then possible that the energy released from the falling knots may be radiated away from these knots and into the surrounding environment (as in Haerendel & Berger 2011). In the quiet Sun, the heating power requirement is about  $10^5 \text{ erg cm}^{-2} \text{ s}^{-1}$  (Withbroe & Noyes 1977). If we roughly assume that the area of the quiet Sun is equivalent to the surface area of the whole Sun, the gravitational energy lost by these falling knots amounts to 1/2000 of the energy needed to heat the quiet Sun.

It is worth noting that the individual knots may continue to fall after they disappeared according to the  $\text{H}_\alpha$  linecore image. This is supported by the fact that the knots did not display any significant decrease in the falling speed before they disappeared in our  $\text{H}_\alpha$  image. The line width of the NVST  $\text{H}_\alpha$  prefilter is  $0.25 \text{ \AA}$ , which means that the knots disappear on the  $\text{H}_\alpha$  images when the line of sight (LOS) speed of the knots exceeds  $5 \text{ km s}^{-1}$ . During the 5 hr of observations, the horizontal velocity of knots on the image plane was often more than  $5 \text{ km s}^{-1}$ . Assuming that the LOS velocity may reach the same order of magnitude as the horizontal velocity on the plane of the  $\text{H}_\alpha$  images, we suggest that a significant portion of the knots may experience further downward motion not captured in the  $\text{H}_\alpha$  observations. Moreover, it is also worth drawing attention to the differing behavior of the knots above and below a height of 7 Mm. Below 7 Mm it was clear in Section 3 that the knots

experienced strong decelerations as they approached the surface, however those above 7 Mm appear to have maintained a constant velocity. Therefore, considering instead that these knots may have traversed a significant height, they could release gravity potential energy of the order  $3.1 \times 10^{22} \text{ erg}$ , which is equivalent to a potential energy loss rate of  $1.9 \times 10^{18} \text{ erg s}^{-1}$ . Hence, the energy loss rate from this studied prominence could increase to 1/320 of the heating power requirement for the corona in the quiet Sun. Of course, this can be viewed as an ideal upper limit for the loss rate of gravitational potential energy from the knots in the prominences, and corresponding conversion to dissipated thermal energy. Indeed, the observation from off-band  $\text{H}_\alpha$  wavelengths will allow us to further constrain this conclusion with an ability to detect the descending knots that have an LOS speed greater than  $5 \text{ km s}^{-1}$ .

The prominences are not ubiquitous structures and are therefore unlikely to be responsible for heating the entire quiet Sun. However, the prominences same as or larger than the one present here are often observed in the solar limb. Moreover, only the prominence whose spine is almost parallel to the plane of sky could show its details in the image. When the spine of the prominence runs along the LOS, the prominence appears as a very narrow structure on the edge of the Sun. Furthermore, there are small prominences that may not be clearly observed. Of course, prominences often appear as filaments on the solar disk and a lot of filaments with various scales can be observed simultaneously. Taken together, it is likely that a considerable number of prominences exist in the solar corona at the same time. Therefore, within the bounds of our assumptions, the possibility of ubiquitous, falling knots may well contribute in a nonnegligible way to the local heating of the surrounding corona.

## 5. Conclusion

We have investigated the descending knots in a solar prominence observed by NVST. Our major findings and their implications are as follows.

1. Using the Demon method, we found that most of the detected knots fell with an approximately constant speed.
2. By analyzing the distributions of the downward velocities for these falling knots, we suggested that the constant velocity is consistent with the theory of plasma packets slipping across horizontal magnetic fields.
3. Assuming that the gravity potential energy lost by these detected falling knots could convert to the thermal energy of the corona, we speculated that released potential energy by the falling knots could heat the surrounding corona.

A robust estimation of the density of the knots in the prominence will allow us to precisely estimate the loss rate of the gravitational potential of the falling plasma. Additional modeling work is also required in order to reveal how the interaction between the falling dense plasma and the magnetic field generates the Alfvén wave, dissipation of which is capable of contributing to the heating of the local corona.

The authors sincerely thank the anonymous referee for detailed comments and useful suggestions for improving this manuscript. Y.B. is supported by the Natural Science Foundation of China under grants 11873088 and U1831210, and Young



Elite Scientists Sponsorship Program by CAST. T.L. is supported by the National Key Research and Development Program of China (2019YFA0405000). This work is also supported by the Natural Science Foundation of China under grants 11633008, 11773072, 11873027, 11933009, 11773039, 11933009, 11703084, and 11763004, CAS grant QYZDJ-SSW-SLH012, the grant associated with the project of the Group for Innovation of Yunnan Province, and the project supported by the Open Research Program of the Key Laboratory of Solar Activity of Chinese Academy of Sciences (grant No. KLSA201710). This work used the DAVE/DAVE4VM codes developed by the Naval Research Laboratory. The NASA/*SDO* and GONG data used here are courtesy of the AIA and GONG science teams.

## Appendix

### A.1. Uncertainty of DAVE and Demon Velocities

In order to ascertain the uncertainty in the DAVE and Demon velocities, an experiment was performed on synthetic data sets. We created a synthetic image by shifting one of the  $H_\alpha$  images a random number of pixels away from its original

position in both the horizontal and vertical directions. The random number was chosen to range from 0.5 to 4.5 pixels, since the velocities of detected knots range from 5 to 50  $\text{km s}^{-1}$ . Between the original and the shifted image, all of the knots were moved at a known distance. The procedure was repeated a total of 200 times. Accordingly, we could compare the 200 sets of known displacements of each knot and the corresponding DAVE or Demon found displacement. If the found displacements are equal to the known displacements, the points should scatter around the  $x = y$  line in the scatter diagram (Figure 6). For most of knots, the DAVE found displacements were lower than the known displacements (Figure 6(a)), indicating that the DAVE method often underestimates the velocities of these knots. However, the differences between the Demon found displacements and the known displacement were always lower than 0.18 pixels (Figure 6(b)). This implies that the errors of the velocities measured by Demon amount to 2  $\text{km s}^{-1}$ . We then suggest that the Demon method could provide better estimated velocities of the knots that are detected in the  $H_\alpha$  image.

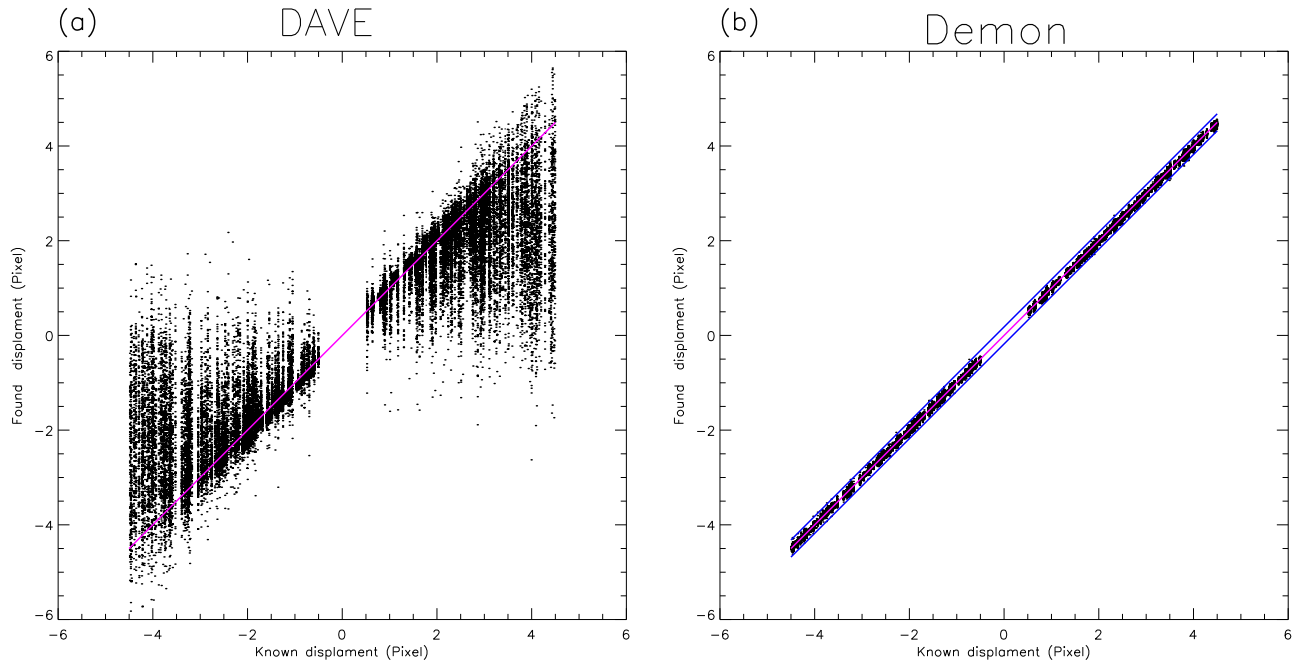


**Figure 6.** Plot of the known velocities and the found velocities of each detected knots. In panels (a) and (b), the velocities are found based on the methods of DAVE and Demon, respectively. In each panel, the magenta line is an  $x = y$  line passing through the origin. In panel (b), the blue lines are parallel to and have a space of 0.18 pixels with the magenta line.

## ORCID iDs

Yi Bi  <https://orcid.org/0000-0002-5302-3404>  
 Bo Yang  <https://orcid.org/0000-0002-1322-9061>  
 Ting Li  <https://orcid.org/0000-0001-6655-1743>  
 Kaifan Ji  <https://orcid.org/0000-0001-8950-3875>

## References

- Antiochos, S. K., MacNeice, P. J., Spicer, D. S., et al. 1999, *ApJ*, 512, 985  
 Berger, T. E., Shine, R. A., Slater, G. L., et al. 2008, *ApJL*, 676, L89  
 Berger, T. E., Slater, G., Hurlburt, N., et al. 2010, *ApJ*, 716, 1288  
 Chae, J. 2010, *ApJ*, 714, 618  
 Chae, J., Ahn, K., Lim, E.-K., Choe, G. S., & Sakurai, T. 2008, *ApJL*, 689, L73  
 Cirtain, J. W., Golub, L., Winebarger, A. R., et al. 2013, *Natur*, 493, 501  
 Close, R. M., Parnell, C. E., Longcope, D. W., et al. 2005, *SoPh*, 231, 45  
 Engvold, O. 1976, *SoPh*, 49, 283  
 Engvold, O. 2015, in *Solar Prominences, Astrophysics and Space Science Library*, Vol. 415, ed. J. C. Vial & O. Engvold (Cham: Springer), 31  
 Feng, S., Deng, L. H., Shu, G. F., et al. 2012, in *IEEE Fifth Int. Conf. on Advanced Computational Intelligence (ICACI)* (New York: IEEE), 626  
 Freed, M. S., McKenzie, D. E., Longcope, D. W., et al. 2016, *ApJ*, 818, 57  
 Haerendel, G., & Berger, T. 2011, *ApJ*, 731, 82  
 Heinzel, P., Bommier, V., & Vial, J. C. 1996, *SoPh*, 164, 211  
 Heinzel, P., Gunár, S., & Anzer, U. 2015, *A&A*, 579, A16  
 Hillier, A., Hillier, R., & Tripathi, D. 2012, *ApJ*, 761, 106  
 Kaneko, T., & Yokoyama, T. 2018, *ApJ*, 869, 136  
 Karpen, J. T., Antiochos, S. K., Hohensee, M., et al. 2001, *ApJL*, 553, L85  
 Keppens, R., Xia, C., & Porth, O. 2015, *ApJL*, 806, L13  
 Labrosse, N., Heinzel, P., Vial, J.-C., et al. 2010, *SSRv*, 151, 243  
 Lemen, J. R., Title, A. M., Akin, D. J., et al. 2012, *SoPh*, 275, 17  
 Li, D., Shen, Y., Ning, Z., et al. 2018, *ApJ*, 863, 192  
 Liu, H., Yang, Y.-F., Shang, Z.-H., & Li, R.-X. 2018, *AR&T*, 15, 151, [http://html.rhhz.net/Jwk\\_twyjyjs/html/20180203.htm](http://html.rhhz.net/Jwk_twyjyjs/html/20180203.htm)  
 Liu, W., Berger, T. E., & Low, B. C. 2012, *ApJL*, 745, L21  
 Liu, Z., & Beckers, J. M. 2001, *SoPh*, 198, 197  
 Liu, Z., Xu, J., Gu, B.-Z., et al. 2014, *RAA*, 14, 705  
 Low, B. C., Berger, T., Casini, R., et al. 2012, *ApJ*, 755, 34  
 Mackay, D. H., & Galsgaard, K. 2001, *SoPh*, 198, 289  
 Mackay, D. H., Karpen, J. T., Ballester, J. L., et al. 2010, *SSRv*, 151, 333  
 McIntosh, S. W., de Pontieu, B., Carlsson, M., et al. 2011, *Natur*, 475, 477  
 Morgan, H., & Druckmüller, M. 2014, *SoPh*, 289, 2945  
 November, L. J., & Simon, G. W. 1988, *ApJ*, 333, 427  
 Oliver, R., Soler, R., Terradas, J., et al. 2014, *ApJ*, 784, 21  
 Parker, E. N. 1988, *ApJ*, 330, 474  
 Pesnell, W. D., Thompson, B. J., & Chamberlin, P. C. 2012, *SoPh*, 275, 3  
 Samanta, T., Tian, H., Yurchyshyn, V., et al. 2019, *Sci*, 366, 890  
 Schuck, P. W. 2006, *ApJ*, 646, 1358  
 Shen, Y., Liu, Y., Liu, Y. D., et al. 2015, *ApJL*, 814, L17  
 Thirion, J.-P. 1988, *Med. Image Anal.*, 2, 243  
 Thurgood, J. O., Morton, R. J., & McLaughlin, J. A. 2014, *ApJL*, 790, L2  
 Weberg, M. J., Morton, R. J., & McLaughlin, J. A. 2018, *ApJ*, 852, 57  
 Withbroe, G. L., & Noyes, R. W. 1977, *ARA&A*, 15, 363  
 Xia, C., & Keppens, R. 2016, *ApJ*, 823, 22  
 Xiang, Y.-y., Liu, Z., & Jin, Z.-y. 2016, *NewA*, 49, 8  
 Xu, Z., Jin, Z. Y., Xu, F. Y., & Liu, Z. 2014, in *IAU Symp. 300, Nature of Prominences and their role in Space Weather*, ed. B. Schmieder, J.-M. Malherbe, & S. T. Wu (Cambridge: Cambridge Univ. Press), 117  
 Yang, Y.-F., Lin, J.-B., Feng, S., et al. 2014, *RAA*, 14, 741  
 Zhang, J., Zhang, B., Li, T., et al. 2015, *ApJL*, 799, L27  
 Zirker, J. B., & Engvold, O. 2017, *PhT*, 70, 36  
 Zirker, J. B., Engvold, O., & Martin, S. F. 1998, *Natur*, 396, 440  
 Zuiderveld, K. 1994, in *Graphic Gems IV*, ed. P. S. Heckbert (San Diego, CA: Academic ), 474